Journal of Engineering Mathematics (2025) 152:12
https://doi.org/10.1007/s10665-025-10451-w

Phase separation of a binary fluid mixture under external forcing

Mark Fasano[1] · Javier A. Diez[2] · Ofer Manor[3] · Lou Kondic[1] · Linda Cummings[1]

Received: 18 December 2024 / Accepted: 15 April 2025 / Published online: 22 May 2025

Abstract

We present a simplified, thermodynamically consistent model of the phase separation of a binary fluid mixture under the effects of a conservative volume force that drives fluid flow. Enforcing conservation of mass provides advection–diffusion equations for the concentrations of the individual components. We propose Darcy-type laws for the velocity and flux of each component, that ensure a nonincreasing free energy functional consistent with the second law of thermodynamics in an isothermal setting. The model is closed by prescribing a free energy in accordance with the Cahn–Hilliard and Flory–Huggins theories. A linear stability analysis of the unforced model yields the range of initial concentrations for which instability occurs and the linear growth rate of perturbations, which are numerically confirmed. We provide fully nonlinear numerical solutions to the model in the specific case of a silicone oil–water mixture, where the conservative force is generated by gravity, or by a surface acoustic wave (SAW) propagating through the underlying substrate. In agreement with recent experimental results, we find that increasing the SAW amplitude or decreasing the SAW

✉ Mark Fasano
mf326@njit.edu

Javier A. Diez
jdiez@ifas.exa.unicen.edu.ar

Ofer Manor
manorO@technion.ac.il

Lou Kondic
kondic@njit.edu

Linda Cummings
Linda.Cummings@njit.edu

[1] Department of Mathematical Sciences, NJIT, University Heights, Newark, NJ 07102, USA

[2] Instituto de Física Arroyo Seco (CIFICEN-CONICET-CICPBA), Universidad Nacional del Centro de la Provincia de Buenos Aires, Pinto 399, 7000 Tandil, Buenos Aires, Argentina

[3] Department of Chemical Engineering, Technion - Israel Institute of Technology, 32000 Haifa, Israel

attenuation length speeds up total phase separation. This provides a proof-of-principle for modeling phase separation due to the effects of a SAW, within the limitations of our model.

Keywords Cahn–Hilliard dynamics · Phase separation · Surface acoustic waves

1 Introduction

Many processes involve binary fluid mixtures undergoing a phase separation process, including metal alloys heated via laser pulses [1], greywater recovery [2], the formation of membraneless protein granules in embryos of roundworms [3], and even tumor growth [4]. Thus, the study of mixtures separating into distinct phases (spinodal decomposition) has received significant attention over the years. The diffuse-interface approach, where the interface between two immiscible fluid phases is considered to have a small but finite thickness, was first introduced by van der Waals and Rayleigh [5]. Cahn and Hilliard [6] made another major advance when they accurately described the free energy in a mixture as dependent on both local concentration and local concentration gradients. They also extended van der Waals' hypothesis to time-dependent situations by approximating interfacial diffusion fluxes as being proportional to chemical potential gradients [7]. Notably though, the standard Cahn–Hilliard model does not account for ambient fluid flow, important in many practical situations.

Several methods to incorporate fluid flow into the Cahn–Hilliard model have since been proposed, such as coupling the system to Darcy's Law [4, 8–10], or to the Stokes [11] or Navier–Stokes equations [12]. The Darcy approach was used to model two-dimensional multiphase flow in a Hele–Shaw cell [8–10] where the fluid mixture is trapped between two parallel plates. This is very similar to the setup considered in the present work, where we have a binary mixture trapped in a closed cell; hence a Darcy-type model may provide an appropriate framework. A generalized Darcy Law was also successfully used to model tumor growth in which the tumor cells and host organism cells are treated as constituent fluid components that can migrate, while undergoing phase separation [4]. One can justify such a model in this more general setting on the basis that, with a mixture of several phases present, each fluid must travel through the other fluid(s), which exert mutual drag, thus one fluid experiences the other(s) as a porous medium.

In the Stokes flow approach, the two-phase system is modeled by coupling the concentration equation for one of the phases to the Stokes equations (in the particular example cited [11], a mixture of two immiscible liquids is confined in a closed cell and subjected to shearing). Coupling the Cahn–Hilliard equation to the full Navier–Stokes equations produces the most complete (and complicated) model. Náraigh and Thiffeault [12] considered a simplified version of this problem: phase separation in asymptotically-thin free surface fluid films comprising two density- and viscosity-matched fluid phases; the resulting equations couple the evolving free surface fluid film height to the film-averaged phase concentration. The case of fluid mixtures where the components have contrasting densities and viscosities is still an active area of interest; Ding et al. [13] have provided one possible framework for this scenario.

Within the thin-film context studied by Náraigh and Thiffeault [12], an alternative gradient dynamics formulation has been investigated by multiple authors; see Thiele [14] for a recent review. The models discussed in this work have applications ranging from describing the free surface evolution of two-layer flows to solutions (e.g., mixtures or suspensions), with or without surface activity. The main idea is to use Onsager's variational principle to derive a general thin-film equation in the form of a gradient dynamics for one (or multiple) conserved order parameter(s). The equations arising from this approach have been shown to be equivalent to the standard thin-film equations that result from the full Navier–Stokes equations in corresponding limiting situations. Interestingly, in certain limits, the general gradient dynamics approach is broken and the question of whether these systems can result in unphysical behavior remains unanswered [15].

Avoiding such difficulties associated with free surface flows, the goal of the present paper is to model the phase separation of an oil–water mixture trapped in a closed cell under the influence of external forcing. While the model we develop allows for inclusion of fairly general (conservative) forcing, motivated by potential applications in greywater recycling, we mostly focus here on forcing due to a *surface acoustic wave* (SAW) propagating through one side of the cell (the substrate). Recent experimental work [16] suggests that this may be an inexpensive and efficient way to hasten the separation of mixtures of silicone oils and water. In those experiments, a mm-scale drop of oil–water emulsion is placed on a planar lithium niobate actuator, a few cm long, with an interdigitated transducer (IDT) at one end. When voltage is applied across the IDT, a SAW is generated along the substrate, which drives flow in the droplet. Under these conditions, the initially well-mixed drop is observed to phase-separate rapidly, so that a thin film of oil coats the surface of the drop, including the contact line. After a sufficient time period, a film of oil (of order 10 μm) is extracted from the stationary droplet and begins to travel in opposition to the propagating wave. Similar setups with free surface droplets or films have also been examined experimentally and theoretically by other authors [17–19]; it has been found that fluid dynamics and phase separation depend not only on the physical properties of the fluids that form the emulsion, but also on the size and composition of the droplet and the thickness of the oil film that forms [20].

As the earlier discussion of modeling phase separation coupled to fluid dynamics makes clear, these free surface flow setups are quite complex to model, even within the thin-film approximation; and here, in addition to the questions that remain about the appropriateness of that approach, one needs to account also for the external forcing. Hence, rather than attempting to model the full experimental configuration, we adopt a less ambitious approach in which we model the flow and forced phase separation in a closed cell, so as to ignore the complications of free surface dynamics for now. We also employ a simplified Darcy-type model for the fluid dynamics [4, 8–10], which models the external force driving the flow as a conservative volume force (described by a scalar potential), which acts on both phases in the mixture, but which they experience differently due to their different densities and viscosities. We consider the potential to derive from two distinct possible sources: the potential from a SAW propagating through the underlying substrate *or* a gravitational potential. The Darcy-type expressions for the component velocities are used in conjunction with

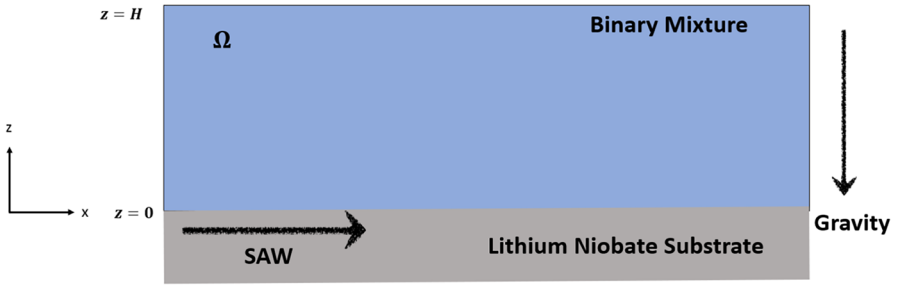

Fig. 1 Schematic of the physical setup. A homogeneous binary mixture is initially at rest in a closed cell occupying spatial domain Ω, sitting atop a flat substrate. The mixture is then excited by a conservative volume force acting parallel and/or perpendicular to the substrate, leading to enhanced phase separation

conservation of mass (volume) arguments to derive a thermodynamically consistent system for the concentration profile of the binary mixture and the underlying pressure field.

The remainder of this paper is structured as follows: In Sect. 2, we present the derivation of our model for a general binary mixture with components that have distinct viscosities (which, in the approach we take, materialize as distinct component mobilities) and densities. In Sect. 3, we present results for a specific application of this model to a binary mixture of silicone oil and water. We include results with a gravitational forcing potential function as well as the forcing potential arising from a SAW propagating through the boundary at $z = 0$. Finally, in Sect. 4, we present our conclusions.

2 Forced phase separation in a closed cell

To derive the general model, we first propose conservation laws for the volume concentrations of both components. Then, following the approach of Wise et al. [4], we determine thermodynamically consistent velocity and flux equations for each component (i.e., generalized Darcy laws for each phase of the mixture). Finally, we prescribe an associated free energy to the mixture following the Cahn–Hilliard theory [6], but with an additional contribution due to the conservative body force. Boundary conditions for our system arise during the derivation of velocity and flux expressions, which close the model. This section concludes with linear stability analysis (LSA) of the system, in the absence of forcing.

2.1 Modeling preliminaries

We consider an incompressible binary mixture, comprising components A and B, in a fixed rectangular cell Ω with solid walls, as depicted in Fig. 1. Then, a given volume of the mixture, V_{m}, can be decomposed as

$$V_{\mathrm{m}} = V_A + V_B, \tag{1}$$

where V_A and V_B are the respective volumes of the two components in the mixture, and we can define the volume concentrations of each phase,

$$\phi_A = \frac{V_A}{V_\mathrm{m}}, \qquad \phi_B = \frac{V_B}{V_\mathrm{m}}, \tag{2}$$

from which it follows that the no-voids constraint, $\phi_A + \phi_B = 1$, must be satisfied. We further define the density and the mass-averaged velocity of the mixture as

$$\rho_\mathrm{m} = \rho_A\phi_A + \rho_B\phi_B, \qquad \vec{u}_\mathrm{m} = \rho_\mathrm{m}^{-1}\Big(\rho_A\phi_A\vec{u}_A + \rho_B\phi_B\vec{u}_B\Big), \tag{3}$$

where ρ_i and $\vec{u}_i$ $(i = A, B)$ are the component densities and velocities, respectively. The incompressibility condition for the mixture is then

$$\nabla \cdot \vec{u}_\mathrm{m} = 0, \tag{4}$$

while mass conservation for the mixture is represented by

$$\frac{\partial \rho_\mathrm{m}}{\partial t} + \vec{u}_\mathrm{m} \cdot \nabla \rho_\mathrm{m} = 0. \tag{5}$$

In what follows, we will solely consider the case of constant component densities, ρ_A and ρ_B. Note, however, that the mixture density ρ_m in Eq. (3) is not constant due to its dependence on the phase concentration variables ϕ_A, ϕ_B.

2.2 Model derivation

In this section, we derive the model that we use to describe the phase separation of a binary mixture in a closed cell (represented by a finite computational domain Ω), excited by an external conservative volume force to which the two phases may respond differently. We begin by utilizing basic conservation arguments to write down convection–diffusion equations for the component concentrations, then follow the approach of Wise et al. [4] and use arguments based on energetics to determine thermodynamically consistent velocity and flux equations for each component. The model is closed by prescribing a free energy for the system, which we do in accordance with the Cahn–Hilliard theory [6].

2.2.1 Conserved quantities

Since we consider a closed-cell geometry, the mass of the entire two-phase mixture should be conserved. Further, because there is no chemical reaction taking place, the mass of each of the components must be conserved. It follows that the concentration of each component must satisfy a convection–diffusion equation of the form

$$\frac{\partial(\rho_i\phi_i)}{\partial t} + \nabla \cdot (\rho_i\vec{u}_i\phi_i) + \nabla \cdot \vec{J}_i = 0, \qquad i = A, B, \tag{6}$$

where the second term represents the convective flux, while $\vec{J}_i$ is the diffusive flux of component i. On summing Eq. (6), we see that conservation of mass of the mixture, given by Eq. (5), is satisfied only if $\vec{J}_A + \vec{J}_B = \vec{C}$, where $\vec{C}$ is a constant. To further satisfy the no-penetration boundary condition imposed later in Eq. (15), we must require that $\vec{C} = 0$ which we assume in everything that follows by enforcing $\vec{J}_B = -\vec{J}_A$. We make the additional assumption that the component densities, ρ_i, are constant, and we utilize the no-voids constraint to define a single concentration variable ϕ,

$$\phi_A \equiv \phi, \quad \phi_B \equiv 1 - \phi. \tag{7}$$

Then, replacing the conservation equation for component B by the sum of the conservation equations for both components (see Eq. (6)), the system can be equivalently written as

$$\frac{\partial \phi}{\partial t} + \nabla \cdot \left(\vec{u_A} \phi + \frac{1}{\rho_A} \vec{J}_A \right) = 0, \tag{8}$$

$$\nabla \cdot \left(\vec{u}_A \phi + \vec{u}_B (1 - \phi) \right) + \left(\frac{1}{\rho_A} - \frac{1}{\rho_B} \right) \nabla \cdot \vec{J}_A = 0. \tag{9}$$

These equations must be solved on the specified computational domain Ω, subject to suitable boundary conditions on the boundary $\partial\Omega$ (discussed further below).

2.2.2 Constitutive laws for component fluxes and velocities

Here, we follow Wise et al. [4], who proposed generalized Darcy-type constitutive equations for the velocities and fluxes of each fluid component, that are thermodynamically consistent with a nonincreasing total free energy. We choose this route over approaches used by other authors (such as Khatavkar et al. [11, 12], who couple a concentration equation with standard fluid momentum equations such as the Stokes or Navier–Stokes equations), for two main reasons: first, a Darcy-type model provides considerable simplification, averting the need to couple Eqs. (8) and (9) to another equation for the mixture velocity; and second, this method has proved successful in applications such as tumor modeling [4].

In their tumor model, Wise et al. introduced a four-phase system, with distinct concentrations for a nutrient-carrying water phase, a host tissue phase, a live tumor-cell phase (which phase-separates from host tissue), and a necrotic tumor-cell phase. Here, we take a specific limit of that model in which only two phases (corresponding to the phase-separating host tissue and live tumor cells) are present, and further modify their model to account for the presence of an external forcing. Hence, following the approach in Wise et al., if we assume a free energy functional that depends only on the component concentrations, $E = E[\phi_A, \phi_B]$, we can derive the following thermodynamically consistent expressions for the velocities and fluxes of the phases:

$$\vec{u}_A = -(q + q_A) \left[\nabla p - 2 \frac{\delta E}{\delta \phi} \nabla \phi \right] - q \rho_{\mathrm{m}} \nabla \psi$$

$$- q_A \left[2(1-\phi)\nabla \frac{\delta E}{\delta \phi} + \rho_A \nabla \psi \right], \tag{10}$$

$$\vec{u}_B = -(q + q_B) \left[\nabla p - 2 \frac{\delta E}{\delta \phi} \nabla \phi \right] - q \rho_{\mathrm{m}} \nabla \psi - q_B \left[\rho_B \nabla \psi - 2\phi \nabla \frac{\delta E}{\delta \phi} \right], \tag{11}$$

$$\vec{J}_A = -\vec{J}_B = -M_B \left(\left(\frac{1}{\rho_A} + \frac{1}{\rho_B} \right) \nabla \frac{\delta E}{\delta \phi} + \left(\frac{1}{\rho_A} - \frac{1}{\rho_B} \right) \left(\nabla p + (1-2\phi) \nabla \frac{\delta E}{\delta \phi} - 2 \frac{\delta E}{\delta \phi} \nabla \phi \right) \right), \tag{12}$$

(see Appendix A for details). Here, q, q_A, q_B are positive mobilities, all with dimensions L^3T/M (specifically, q is the mass-averaged mobility coefficient for the mixture, while q_i is the mobility coefficient for component i); M_B is the diffusive mobility coefficient with dimensions MT/L^3; and p is the underlying pressure in the mixture. We estimate the value of the unknown diffusion mobility coefficient using $M_B = \rho_B^2 q_B$ [21]. Both component velocities contain a Darcy-type term proportional to the gradient of the pressure, and terms that represent the excess force resulting from similar and dissimilar cell–cell interactions (in the language of the tumor model). The diffusive fluxes $\vec{J}_i$ of each component are of equal magnitude and opposite sign to ensure conservation of total volume (which, given our assumption of constant densities, is equivalent to conservation of total mass). Finally, ψ represents the potential of some conservative volume force; the inclusion of terms proportional to $\nabla\psi$ in the component velocities extends the model of Wise et al. [4].

In what follows, we will consider two specific examples, where (i) the forcing is due to gravity; and (ii) the forcing is due to the effects of a SAW propagating through the lower boundary (as considered by Shiokawa et al. [22], and Li et al. [23] in a different context). The forcing in the first case is well studied, and straightforward to model. In the second case, as the wave propagates through the substrate, its amplitude attenuates strongly due to the overlying viscous fluid (much more so than if air surrounded the substrate). This is modeled by a potential that decays exponentially in x. Similarly, the effects of the wave attenuate in the z-direction into the fluid; this is also modeled by an exponential decay in z (albeit with a different attenuation rate constant). Thus, we use for the potential ψ

$$\psi_{\mathrm{g}} = -gz \quad \text{or} \quad \psi_{\mathrm{s}} = (1+\lambda^2)\mathcal{A}^2\omega^2 \mathrm{e}^{-\alpha(x+\lambda z)}, \tag{13}$$

where for the gravitational forcing ψ_{g}, g is the standard gravitational acceleration with dimensions L/T^2. For the SAW forcing ψ_{s}, $\mathcal{A}$ is the maximum amplitude of the vertical displacements at the surface of the solid substrate due to the propagating SAW, $\omega = 2\pi f$ is the angular frequency of the SAW, α is the SAW attenuation factor in the x-direction (the direction of SAW propagation), and $\lambda\alpha$ is the SAW attenuation factor in the z-direction. See Shiokawa et al. [22] for more details regarding this form of acoustic forcing potential and its derivation.

The SAW attenuation factor is the inverse of the attenuation length ℓ of the SAW for the given substrate-fluid system, and is calculated using [24]

$$\alpha = \frac{1}{\ell} = \frac{\rho_{m,0}}{\rho_s} \frac{c_m}{c_s^2} f, \tag{14}$$

where ρ_s and $\rho_{m,0}$ are the density of the substrate and the initial mixture, while c_s and c_m are the SAW phase velocities in the substrate and the mixture, respectively.

Equations (10)–(13) substituted into Eqs. (8) and (9) form a closed system to be solved on Ω once the free energy E is specified. As is demonstrated in Appendix A, the boundary conditions to be imposed on $\partial\Omega$ arise during the derivation of the expressions for the phase velocities and fluxes and are given below (see Eq. (A.3)):

$$\left(\vec{u}_A \phi + \frac{1}{\rho_A} \vec{J}_A\right) \cdot \hat{n} = 0, \quad \text{on } \partial\Omega, \tag{15}$$

$$\left(\vec{u}_B (1-\phi) - \frac{1}{\rho_B} \vec{J}_A\right) \cdot \hat{n} 0, \quad \text{on } \partial\Omega, \tag{16}$$

$$p = 0, \quad \text{on } \partial\Omega. \tag{17}$$

The first boundary condition (15) above specifies zero flux of both mixture components at all boundaries, ensuring that the total mass (volume) is conserved for each component and hence for the total mixture. The Dirichlet condition imposed on the pressure is to ensure that flow is due not to imposed pressure gradients, but rather to concentration gradients and to the underlying forcing applied.

2.2.3 Associated energy equations

The model is closed by prescribing a free energy for the system, which incorporates all hydrodynamic effects to be considered. According to the Cahn–Hilliard theory, the free energy of the system should be dependent on the free energy of the homogenous system with a given reference concentration and the local free energy density for a compositionally inhomogeneous system [4, 6, 25]. Hence, in a closed, rectangular cell Ω, the total energy of the mixture is

$$E = \int_\Omega \left(f(\phi) + \frac{\epsilon^2}{2} |\nabla\phi|^2 + \rho_m \psi \right) \mathrm{d}\vec{x}. \tag{18}$$

The first term on the right-hand side above represents the bulk energy due to local interactions, while the second term models interfacial energy (interfaces being characterized by concentration gradients) and is the term responsible for the domain coarsening seen in solutions to the standard Cahn–Hilliard equation. The last term is the added energy per unit volume (pressure) due to the conservative volume force, ψ. We note that here $\vec{x} = (x, y, z)$; for the lower dimensional problems studied, we consider the "extra" spatial variables to be a scaling factor to ensure that the correct dimensions are obtained.

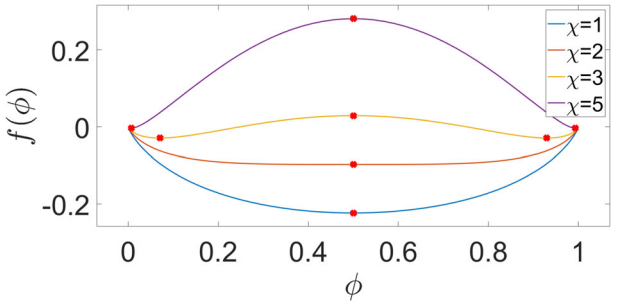

Fig. 2 Shown is the Flory–Huggins logarithmic potential (19) for various values of the interaction parameter, χ. For $\chi \leq 2$, the function has a single minimum at $\phi = 0.5$; these values should be used to model miscible liquids that prefer to stay mixed. For $\chi > 2$, the function has two local minima equally spaced from the center that approach 0, 1, respectively, as χ increases. The critical points for the function are shown by the red dots on each graph; notice the appearance of the two local minima as $\chi > 2$ and how these move closer to the extreme values of ϕ as χ increases further. (Color figure online)

We utilize the Flory–Huggins form [26] for the homogeneous bulk free energy density $f(\phi)$ in Eq. (18),

$$f(\phi) = \bar{E}\Big(\phi \ln(\phi) + (1-\phi)\ln(1-\phi) + \chi\phi(1-\phi)\Big), \qquad \bar{E} = \frac{k_b \mathcal{T}}{V_{\mathrm{m}}}. \quad (19)$$

Here, k_b is Boltzmann's constant, $\mathcal{T}$ is the temperature of the mixture (assumed constant here), and V_{m} is the volume of the mixture in Ω. In this setting, χ is the nondimensional interaction parameter that depends on both phases; it is a mixture-specific parameter that provides the excess energy of the mixing of two components. This function is plotted in Fig. 2 for various values of χ.

This choice of free energy density, which is commonly used in modeling phase separation, guarantees that our solution will remain within physical bounds (i.e., $0 \leq \phi \leq 1$) for an appropriate choice of χ. Specifically, for $\chi > 2$, $f(\phi)$ has two attractive minima, symmetrically placed in the interval $(0, 1)$; the equations evolve so as to minimize the energy E, and thus minimize f as well. As time passes, if the numerical method slightly over- or undershoots the true minima during the evolution, it is attracted back to the desired values within physical bounds. Further, as χ increases, the minima approach $\phi = 0$ and $\phi = 1$, which give rise to a well-delineated phase separation of components in the solution. Note that for $\chi \leq 2$, the function has a single minimum at $\phi = 0.5$; in such situations (not considered here), the well-mixed state is preferred and the phases do not separate. Hence, the choice of $\chi \leq 2$ is appropriate for the case of two miscible liquids. It is commonplace in numerical applications to approximate the above logarithmic function with a quartic double-well polynomial [4, 27, 28], although we do not do that here.

All terms in the integrand of the energy functional $E[\phi]$, defined in Eq. (18), have dimensions of energy per volume. Hence, the coefficient $\bar{E} = k_b \mathcal{T}/V$ in $f(\phi)$ (Eq. (19)) has dimensions $M/(LT^2)$ (energy per volume), while the coefficient ϵ^2 has dimensions ML/T^2. The grouping $\sqrt{\epsilon^2/\bar{E}}$ thus has dimensions of length, and is the

typical thickness of the diffuse interface that forms between the two phases (upon phase separation) predicted by the Cahn–Hilliard model [11].

2.3 Nondimensionalization

We proceed by formulating a nondimensional version of the system. As a length scale, we choose the above-mentioned typical interfacial thickness in the model, based on energy parameters ϵ^2 and $\bar{E}$ [4]. Since this lengthscale is expected to be orders of magnitude smaller than the size of the box containing the mixture, to properly model experimental setups, one should take very large nondimensional numerical domains, which requires significant computational resources.[1] To avoid excessive computational demands, we take the common approach of carrying out simulations using an unphysically-large value for this interfacial thickness lengthscale (on the order of 1 mm), allowing us to simulate three-dimensional experiments on the cm scale within a reasonable computing time.

We base our time scale on the same energy parameters and one of the mobility coefficients, as a measure of the rate at which phase separation is occurring due to energy effects. The application we have in mind is a silicone oil–water mixture, for which the viscosity ratio is approximately 50 : 1. Hence, we expect very different mobilities of the phases, water (phase B) being much more mobile ($q_B \gg q_A$), which motivates the use of the mobility q_B to define the timescale. We note here that the numerical results obtained were verified to be independent of the labeling of the two phases (results not shown). We choose to scale our pressure by $\bar{E}$, defined in Eq. (19); this also provides the natural scaling for the free energy density f. The dimensionless variables are defined as follows:

$$\vec{x} = \sqrt{\frac{\epsilon^2}{\bar{E}}}\hat{\vec{x}}, \quad (\vec{u}_A, \vec{u}_B) = \frac{q_B \bar{E}^{3/2}}{\epsilon}(\hat{\vec{u}}_A, \hat{\vec{u}}_B), \quad p = \bar{E}\hat{p},$$
$$t = \frac{\epsilon^2}{q_B \bar{E}^2}\hat{t}, \quad f = \bar{E}\hat{f}, \quad \psi = \psi_c \hat{\psi}, \tag{20}$$

with all hatted quantities being nondimensional. Here, the scale for the forcing potential, ψ_c, is equal to $(\mathcal{A}\omega)^2$ or $g\sqrt{\epsilon^2/\bar{E}}$ depending on the conservative volume force considered (of dimension L^2/T^2 in either case). We also define nondimensional parameters

$$\kappa = \frac{q}{q_B}, \quad \kappa_1 = \frac{q_A}{q_B}, \quad R_\rho = \frac{\rho_A}{\rho_B}, \quad \Lambda = \frac{\rho_B \psi_c}{\bar{E}}, \quad \mathcal{M} = \frac{M_B}{\rho_B^2 q_B}, \quad \gamma = \alpha\sqrt{\frac{\epsilon^2}{\bar{E}}}, \tag{21}$$

[1] Alternatively, we could choose as a length scale the size of the domain, but this would then require a very fine spatial mesh, at least locally, to resolve the diffuse interface where concentration gradients are large. It is possible that careful matched asymptotic analysis could be utilized to allow for more efficient numerical computation on larger domains than considered here; however, this is beyond the scope of the present work.

and a nondimensional gradient operator, $\hat{\nabla} = (\partial_{\hat{x}}, \partial_{\hat{y}}, \partial_{\hat{z}})$. The parameters κ, κ_1 are mobility ratios and R_ρ is the density ratio of the phases, while Λ can be thought of as a measure of the relative strengths of the conservative volume force and the Flory–Huggins logarithmic potential, and $\mathcal{M}$ is a nondimensional diffusion coefficient. Finally, γ, which only appears when $\psi = \psi_s$, via

$$\hat{\psi}_s = (1 + \lambda^2)e^{-\gamma(\hat{x}+\lambda\hat{z})}, \tag{22}$$

is a ratio between the interfacial thickness and the attenuation length of the SAW in the direction of propagation. Substituting these scalings into Eqs. (8)–(12), the system to be solved numerically is

$$\phi_{\hat{t}} + \hat{\nabla} \cdot \left(\phi \vec{\hat{u}}_A + \frac{1}{R_\rho} \vec{J}_A \right) = 0, \tag{23}$$

$$\hat{\nabla} \cdot \left(\phi \vec{\hat{u}}_A + (1-\phi)\vec{\hat{u}}_B \right) + \left(\frac{1 - R_\rho}{R_\rho} \right) \hat{\nabla} \cdot \vec{\hat{J}}_A = 0, \tag{24}$$

where

$$\vec{\hat{u}}_A = -(\kappa_1 + \kappa)\vec{P} - 2\kappa_1(1-\phi)\hat{\nabla}\mu - \Big(\kappa R_\rho \Lambda \phi + \kappa \Lambda (1-\phi) + \kappa_1 R_\rho \Lambda \Big) \hat{\nabla}\hat{\psi}, \tag{25}$$

$$\vec{\hat{u}}_B = -(1+\kappa)\vec{P} + 2\phi\hat{\nabla}\mu - \Big(\kappa R_\rho \Lambda \phi + \kappa \Lambda (1-\phi) + \Lambda \Big) \hat{\nabla}\hat{\psi}, \tag{26}$$

$$\vec{\hat{J}}_A = -\mathcal{M}\left[\frac{2}{R_\rho} \Big(1 - \phi + R_\rho \phi \Big) \nabla\mu + \left(\frac{1 - R_\rho}{R_\rho} \right) \vec{P} \right], \tag{27}$$

$$\mu = \hat{f}'(\phi) + (R_\rho - 1)\Lambda\hat{\psi} - \hat{\nabla}^2\phi, \tag{28}$$

$$\vec{P} = \hat{\nabla}\hat{p} - 2\mu\hat{\nabla}\phi. \tag{29}$$

In Eq. (28) above, the auxiliary variable

$$\mu = \frac{\delta E}{\delta \phi} \tag{30}$$

can be thought of as the nondimensional chemical potential, as it gives the free energy change on replacing a molecule of one component with that of another component, while $\vec{P}$ in Eq. (29) is a generalized pressure gradient. The nondimensional boundary conditions are

$$\left(\vec{\hat{u}}_A \phi + \frac{1}{R_\rho} \vec{\hat{J}}_A \right) \cdot \hat{n} = 0, \quad \text{on } \partial\Omega, \tag{31}$$

$$\left(\vec{\hat{u}}_B (1-\phi) - \vec{\hat{J}}_A \right) \cdot \hat{n} = 0, \quad \text{on } \partial\Omega, \tag{32}$$

$$\hat{p} = 0, \quad \text{on } \partial\Omega. \tag{33}$$

Henceforth, we will drop the hats, on the understanding that we are working with the nondimensional system above. The dimensional parameters in the problem are listed in Table 1, along with the numerical values used in simulations, the dimensions of the quantity, and a brief description of the parameter's physical meaning. The numerical values listed are for the specific case of a silicone oil–water mixture.

2.4 Linear stability analysis (LSA) without external forcing

When $\Lambda = 0$, no external forcing acts and there are equilibrium solutions to Eqs. (23) and (24), given by $(\phi, p) = (\phi_0, p_0)$, where ϕ_0, p_0 are constants. We can study the stability of these uniform states by imposing small perturbations on ϕ and p of the form

$$\phi(x,t) = \phi_0 + \phi_1 e^{i\vec{k}\cdot\vec{x}+\sigma t}, \tag{34}$$

$$p(x,t) = p_0 + p_1 e^{i\vec{k}\cdot\vec{x}+\sigma t}, \tag{35}$$

where $|\phi_1| \ll \phi_0, |p_1| \ll |p_0|, \vec{k} = (k_x, k_y, k_z)$ is the wavenumber, and σ is the growth rate. By linearizing Eqs. (23) and (24) and assuming a 1D geometry for simplicity, so that $\vec{k}\cdot\vec{x} = k_x x = kx$, we obtain a system of equations for ϕ_1 and p_1 in the form

$$a_{11}\phi_1 + a_{12}p_1 = 0, \tag{36}$$

$$a_{21}\phi_1 + a_{22}p_1 = 0, \tag{37}$$

where the coefficients are given by

$$\begin{aligned} a_{11} = {} & k^4\left(\frac{2\mathcal{M}}{R_\rho^2} - \frac{2\mathcal{M}\phi_0}{R_\rho^2} + \frac{2\mathcal{M}\phi_0}{R_\rho} + 2\phi_0\kappa_1 - 2\phi_0^2\kappa_1\right) + \sigma \\ & + k^2\left(-\frac{2\mathcal{M}f'(\phi_0)}{R_\rho^2} + \frac{2\mathcal{M}f'(\phi_0)}{R_\rho} - 2\phi_0\kappa_1 f'(\phi_0) - 2\phi_0\kappa f'(\phi_0) + \frac{2\mathcal{M}f''(\phi_0)}{R_\rho^2}\right. \\ & \left. - \frac{2\mathcal{M}\phi_0 f''(\phi_0)}{R_\rho^2} + \frac{2\mathcal{M}\phi_0 f''(\phi_0)}{R_\rho} + 2\phi_0\kappa_1 f''(\phi_0) - 2\phi_0^2\kappa_1 f''(\phi_0)\right), \end{aligned} \tag{38}$$

$$a_{12} = k^2\left(\frac{\mathcal{M}(1-R_\rho)}{R_\rho^2} + \phi_0(\kappa_1+\kappa)\right), \tag{39}$$

$$\begin{aligned} a_{21} = {} & k^4\left(\frac{2\mathcal{M}}{R_\rho^2}\left(1 - R_\rho - \phi_0 + 2R_\rho\phi_0\right) - 2\phi_0 - 2\mathcal{M}\phi_0 + 2\phi_0^2 + 2\phi_0\kappa_1 - 2\phi_0^2\kappa_1\right) \\ & + \frac{2k^2}{R_\rho^2}\left(-\left(\mathcal{M}(1-R_\rho)^2 - R_\rho^2(\phi_0 - 1) + R_\rho^2\kappa + R_\rho^2\phi_0\right)f'(\phi_0)\right. \\ & \left. + \left(\mathcal{M}(1 - R_\rho - \phi_0 + 2R_\rho\phi_0 - R_\rho^2\phi_0) + R_\rho^2(\phi_0^2 - \phi_0 + \phi_0\kappa_1 - \phi_0^2\kappa_1)\right)f''(\phi_0)\right), \end{aligned} \tag{40}$$

$$a_{22} = \frac{k^2}{R_\rho^2}\left(\mathcal{M} - 2\mathcal{M}R_\rho + R_\rho^2 + \mathcal{M}R_\rho^2 - R_\rho^2\phi_0 + R_\rho^2\phi_0\kappa_1 + R_\rho^2\kappa\right). \tag{41}$$

Table 1 Dimensional parameters in the problem

Symbol	Numerical value	Dimensions	Description
q	$1.777 \times 10^{-10}\,\mathrm{m^3\,s/kg}$	$\frac{L^3T}{M}$	Mobility coefficient for mixture
q_A	$6.592 \times 10^{-12}\,\mathrm{m^3\,s/kg}$	$\frac{L^3T}{M}$	Mobility coefficient for oil component
q_B	$3.296 \times 10^{-10}\,\mathrm{m^3\,s/kg}$	$\frac{L^3T}{M}$	Mobility coefficient for water component
M_B	$3.2763 \times 10^{-4}\,\mathrm{kg\,s/m^3}$	$\frac{MT}{L^3}$	Diffusion mobility coefficient time scale
$\bar{E}$	$5.057 \times 10^{-1}\,\mathrm{kg/m \times s^2}$	$\frac{M}{LT^2}$	Energy per volume coefficient proportional to $\frac{k_bT}{V}$
ϵ^2	$5.057 \times 10^{-9}\,\mathrm{kg\,m \times s^2}$	$\frac{ML}{T^2}$	Energy per length coefficient
ρ_A	$885\,\mathrm{kg/m^3}$	$\frac{M}{L^3}$	Density of oil component
ρ_B	$997\,\mathrm{kg/m^3}$	$\frac{M}{L^3}$	Density of water component
$\rho_{\mathrm{m},0}$	$941\,\mathrm{kg/m^3}$	$\frac{M}{L^3}$	Density of initial mixture
$\mathcal{A}$	$10^{-9}\,\mathrm{m}$	L	Amplitude of vertical displacements at surface
α	$370\,\mathrm{m^{-1}}$	$\frac{1}{L}$	SAW attenuation factor
ω	$1.257 \times 10^8\,\mathrm{Hz}$	$\frac{1}{T}$	Angular frequency of SAW
g	$9.8\,\mathrm{m/s^2}$	$\frac{L}{T^2}$	Standard gravitational acceleration
f	$2 \times 10^7\,\mathrm{1/s}$	$\frac{1}{T}$	Frequency of SAW
c_m	$1376\,\mathrm{m/s}$	$\frac{L}{T}$	SAW velocity in the mixture
c_s	$3880\,\mathrm{m/s}$	$\frac{L}{T}$	SAW velocity in the substrate

Full list of parameters, the numerical value used for computation, the dimensions of each, and a brief description

Nontrivial solutions exist only when the determinant of coefficients vanishes, giving the dispersion relation for the growth rate as a function of the wavenumber, k, as

$$\sigma(k) = -\frac{2\bar{\mathcal{K}}}{\bar{\mathcal{M}}}k^2\left[k^2 + f''(\phi_0)\right], \tag{42}$$

where we have defined the parameters

$$\bar{\mathcal{M}} = \mathcal{M}(1-R_\rho)^2 + R_\rho^2(1-\phi_0) + R_\rho^2(\phi_0\kappa_1 + \kappa) > 0, \tag{43}$$

$$\begin{aligned}\bar{\mathcal{K}} = {} & \kappa R_\rho^2(1-\phi_0)\phi_0^2 + \kappa_1 R_\rho^2\phi_0\left[(1-\phi_0)(1+\kappa(1-\phi_0)) + \mathcal{M}\right] \\ & + \mathcal{M}\left[\kappa\left(1-(1-R_\rho)\phi_0\right)^2 + 1 - \phi_0\right] > 0,\end{aligned} \tag{44}$$

(that $\bar{\mathcal{M}}, \bar{\mathcal{K}} > 0$ can be inferred from the fact that $0 < R_\rho < 1$ for the oil–water mixtures considered here, and also $0 < \phi_0 < 1$). Clearly, the critical wavenumber is given by Eq. (42) as

$$k_c = \sqrt{-f''(\phi_0)}; \tag{45}$$

if $k_c \in \mathbb{R}$, then perturbations with wavenumbers in the range $0 < k < k_c$ will be unstable. Figure 3a shows the dispersion relation Eq. (42) for different values of ϕ_0, using the parameter values from Table 1. From these results we can conclude that, for the chosen parameter values, phase-separation instability occurs for values of ϕ_0 in the range $0.211 < \phi_0 < 0.789$. Thus, a perturbation of the concentration field with an initial concentration $\phi_0 \in (0.211, 0.789)$ will grow in time with growth rate given by Eq. (42) if the perturbation wavenumber, k, lies in the unstable range.

Further, we find the wavenumber of maximum growth, $k_{\max}$, and the corresponding growth rate to be

$$k_{\max} = \sqrt{-\frac{f''(\phi_0)}{2}} \quad \Longrightarrow \quad \sigma(k_{\max}) = \frac{\bar{\mathcal{K}}f''(\phi_0)^2}{2\bar{\mathcal{M}}} = \frac{2\bar{\mathcal{K}}}{\bar{\mathcal{M}}}k_{\max}^4. \tag{46}$$

This prediction is verified in Fig. 3b where the maximum growth rate times t ($\sigma(k_{\max}) \times t$) is plotted (red dashed lines) alongside the growth rates obtained by numerically solving the unforced model, for three cases: $\phi_0 = 0.355$ (black solid line), 0.5 (blue solid line), and 0.75 (green solid line). To calculate the results for a given value of ϕ_0, we compute the normalized amplitude of the concentration perturbation at each time step as the maximum of ϕ minus the minimum of ϕ over the spatial domain (which defines the amplitude A), divided by the initial amplitude of the perturbation of ϕ_1 (which defines the initial amplitude, A_0). As expected, we see good agreement between the LSA and our (unforced) simulations at short times when we are in the linear growth regime; after this, nonlinear effects begin to play a role and the LSA prediction ceases to hold. The results also illustrate the point noted above, that a dilute mixture (in either phase) leads to a much smaller growth rate than a 1:1 mixture.

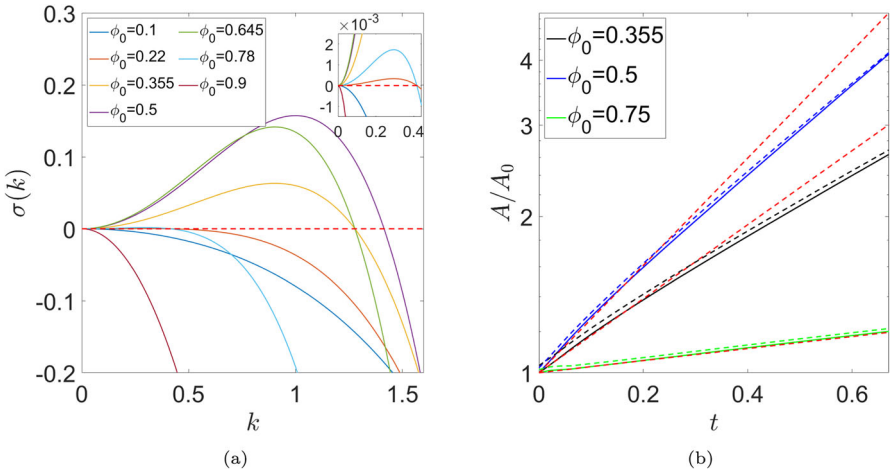

(a) (b)

Fig. 3 **a** The dispersion relation as a function of wavenumber, $\sigma(k)$, with the parameter values in Table 1 and initial concentration values given by the legend. The system is maximally unstable for mixtures containing equal amounts of each phase ($\phi_0 = 0.5$) and becomes more stable as the initial mixture becomes more pure in either phase. The inset shows that for $\phi_0 = 0.22$ (orange) and $\phi_0 = 0.78$ (cyan), we have a very small band of unstable wavenumbers; these values are the bounds of the unstable regime with respect to ϕ_0. **b** Amplitude growth of ϕ (numerically calculated) for the case of no external force (solid lines) and external force with $\Lambda_s = 31.135$ (dashed lines) for three different initial concentrations: $\phi_0 = 0.355$ (black), 0.5 (blue), and 0.75 (green). The corresponding red dashed lines are the product of the analytically predicted maximum growth rate and time. (Color figure online)

Since our focus here is on the phase separation instability under forcing, we also in Fig. 3b compare the analytical results for the unforced case with the corresponding numerical predictions for growth rates in the presence of forcing using the SAW forcing potential (22); notice that the presence of this external force causes slightly faster amplitude growth (black, blue, and green dashed lines), which represents a hastening of initial phase separation.

3 Numerical results

All results presented in this section were computed using COMSOL's PDE Coefficient form. This software runs finite element analysis together with error control using a variety of numerical solvers to accurately solve our second-order system. See Appendix B for a description of the numerical method.

We first discuss the physical setup that motivated our study. The main application considered is a silicone oil–water mixture, acted on by a SAW that propagates along one container boundary. Experiments performed utilizing MHz frequency Rayleigh SAWs have associated known parameter values, which we use accordingly [16]. To determine the rest of the parameters, we use the following logic (see Eqs. (20)): we first fix the length scale to 1 mm based on experimental conditions, which allows us to solve for ϵ; we similarly fix the timescale to 60 s and solve for the parameter q_B; we then use this value to fix q_A by requiring the ratios of the component mobilities to

Table 2 Nondimensional parameters in the model

Symbol	Numerical value	Description
κ_1	0.02	Ratio of mobilities of oil and water
κ	0.54	Ratio of mobilities of mass-averaged mixture and water
Λ_g	1.932	Measure of relative strength of gravity and adhesion (interaction) force
Λ_s	31.135	Measure of relative strength of force from SAW potential and adhesion (interaction) force
$\mathcal{M}$	1	Nondimensional diffusion coefficient
R_ρ	0.888	Ratio of component densities
γ	0.037	Ratio between interfacial thickness and attenuation length of SAW in x-direction
χ	3	Interaction parameter from Flory–Huggins theory
λ	2.47	$(\lambda\alpha)^{-1}$ is attenuation length for SAW in z-direction

Full list of nondimensional parameters, the numerical value used for computation, and a brief description

be equivalent to the ratio of the component viscosities (known to be 50 : 1); finally we solve for the mass-averaged mobility q by using the equation below, where we use the initial concentrations so that this parameter has no time dependence (i.e., $\phi = (1-\phi) = 0.5$)

$$q = \phi \frac{\rho_A}{\rho_m} q_A + (1-\phi)\frac{\rho_B}{\rho_m} q_B. \tag{47}$$

The full list of parameter values used (unless otherwise stated) is given in Table 1. The corresponding nondimensional parameters defined in Sect. 2.3 are given in Table 2.

All solutions shown below correspond to solving Eqs. (23)–(29) with boundary conditions (31)–(33). The section is organized as follows: we first present 1D results for the system under the effects of external forcing due to a SAW potential (ψ_s) or due to the gravitational potential (ψ_g) in Sect. 3.1; here, we also present 1D space–time plots for SAWs of different amplitudes and wave attenuation coefficients to better examine the coarsening dynamics seen in all solutions. To explore further the specific influence of acoustic forcing, we then show 2D results for the system subject to SAWs of different amplitudes in Sect. 3.2. Next, we present 3D results showing the evolution of the system under the two different forcing potentials in Sect. 3.3. We conclude in Sect. 3.4 with a discussion of how the SAW forcing amplitude affects the time until total phase separation in our model. The parameter values in Table 2 are used unless otherwise stated. We emphasize that solutions presented here are *either* for the case of gravity *or* SAW forcing, but never for both. Black arrows are included to indicate the direction of the forcing; this can also be determined by referring to Fig. 1.

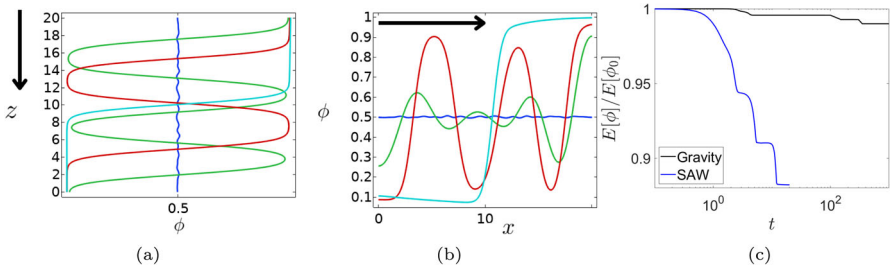

Fig. 4 **a** Snapshots of the solution, ϕ, with gravity acting in the direction of the black arrow are shown at $t = 0, 5, 150, 500$ (blue, green, red, cyan). **b** Snapshots of the solution, ϕ, with a SAW potential applied of amplitude $\mathcal{A} = 1$ nm in the direction of the black arrow are shown at $t = 0, 1, 2.5, 14$ (blue, green, red, cyan). (c) The normalized free energy, $E[\phi]/E[\phi_0]$, calculated at each time step for both simulations. In (a) and (b), the final times shown correspond to the steady state solutions, and the arrows represent the directions of gravity, and the propagating SAW, respectively. (Color figure online)

3.1 Results on a 1D spatial domain

To gain insight into the system behavior, we first study the 1D problem with the following initial conditions:

$$\phi(x,0) = \phi_0 + \sum_{j=1}^{N}\left(A_j \cos\left(\frac{2\pi j}{W}x\right) + B_j \sin\left(\frac{2\pi j}{W}x\right)\right), \qquad 0 \le x \le W, \quad (48)$$

$$p(x,0) = p_0 + \sum_{j=1}^{N}\left(C_j \cos\left(\frac{2\pi j}{W}x\right) + D_j \sin\left(\frac{2\pi j}{W}x\right)\right), \qquad 0 \le x \le W, \quad (49)$$

where $\phi_0 = 0.5$, $p_0 = 0$, $N = 20$, and $W = 20$ is the length of the computational domain in the simulation (corresponding to 2 cm). The coefficients A_j, B_j, C_j, and D_j are random numbers uniformly distributed in $(-\delta, \delta)$ (we use $\delta = 0.001$), so that the initial state is very nearly uniform. The corresponding solutions for ϕ are shown in Fig. 4: in pane (a), the mixture is subjected to a gravitational potential; whereas in pane (b), it is subjected to an acoustic potential, see Eq. (13). For the case of a gravitational potential, note that we take $x \to z$ in the initial conditions given by Eqs. (48)–(49) and consider the dependent variables varying only with z and t. Further, for the case of an acoustic potential, we take $\lambda = 0$ to remove any variations in z and in that way consider a strictly 1D problem (dependent variables varying only in x and t).

The dynamics are qualitatively similar in both cases. Initially, the mixture rapidly separates into its constituent phases creating small internal (nearly) pure phase domains. These domains then coarsen over time until a single domain of each phase exists, separated by a diffuse interface; the coarsening dynamics are a result of the longer-range molecular interactions modeled by the Cahn–Hilliard formulation. In the case of gravity, the buoyancy effect is observed in which the less dense fluid phase (oil) rises to occupy the domain $10 < z < 20$, atop the denser water phase. For the SAW forcing, the oil again ends up in the right-hand side of the computational domain ($x > 10$); this may be attributed to the fact that the forcing arising from ψ_s

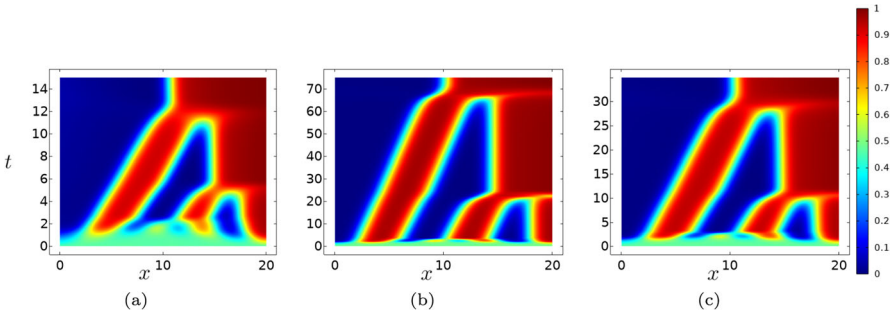

Fig. 5 Space–time plots showing evolution of the concentration patterns of the mixture with the potential from a SAW acting on the system. All parameter values used correspond to Table 2 except: **a** $\Lambda_s = 31.14, \gamma = 0.037$; **b** $\Lambda_s = 31.14, \gamma = 0.0037$; **c** $\Lambda_s = 11.21, \gamma = 0.037$. Note, the steady states are reached for each of the cases by the final time shown. Here, and in all subsequent plots, red indicates pure oil and blue pure water. (Color figure online)

(see Eq. (13)) acts on both components in the $(-x)$-direction, but due to the different densities and mobilities of the two phases they experience the forcing differently: the water phase ends up in the left-hand side of the computational domain $0 < x < 10$, with the oil displaced to the region $10 < x < 20$. A notable difference between the two simulations is the time to reach final equilibrium, which differs significantly for the two forcing types. All nonzero SAW amplitudes examined ($\mathcal{A} > 0$ in Table 1) greatly accelerate the phase separation observed, much more so than gravitational effects.

This observation is further confirmed by pane (c) of Fig. 4, where we plot the normalized free energy functional calculated at each time step: in agreement with our result in Appendix A, we obtain a nonincreasing functional for both simulations. The total free energy is dependent on the conservative volume force itself (see Eq. (18)); hence, a comparison between the amount of energy in the final solution is not appropriate, but the plot confirms that our solutions do in fact evolve to minimize the free energy functional, and that the coarsening process is much faster for the SAW than for gravitational forcing. The plot also shows clearly when a coarsening event is taking place, as such events correspond to large abrupt decreases in the energy.

Figure 5 shows a different set of solutions with an acoustic potential applied to the trapped mixture, for three combinations of values for the parameters Λ_s and γ (see Eqs. (20), (21) and Table 2). The evolution is shown as a space–time plot in each case, with the time domains in plots ending when the solution reaches its steady state. Panes (a) and (b) show cases corresponding to a SAW amplitude of $\mathcal{A} = 1$ nm, but SAW attenuation lengths that differ by a factor of ten (pane (a) uses the default attenuation length from Table 1, for pane (b) it is ten times longer), while pane (c) shows the case of a smaller SAW amplitude $\mathcal{A} = 0.6$ nm with the default attenuation length.

A comparison of panes (a) and (c) shows that increasing the SAW amplitude leads to a significant speed up in phase separation, evident from the time it takes each simulation to achieve complete phase separation (note the different vertical scales in the plots). To compare pane (b), recall that γ is the ratio of the length scale (thickness of the interface separating the phases) and the SAW attenuation length for the system. Thus, assuming interfacial thickness to be fixed, we can interpret decreasing γ as

increasing the attenuation length of the SAW. Comparing panes (a) and (b) we see that decreasing γ leads to an increase in the time to total phase separation (for fixed SAW amplitude). This may be attributed to the fact that a shorter attenuation length means that more of the energy from the propagating SAW is being absorbed by the mixture, leading to quicker phase separation (a SAW that attenuates only slowly loses very little energy to the mixture).

These space–time plots also allow us to better understand the early and intermediate dynamics of the 1D solutions, specifically how the coarsening of like domains occurs. The period of initial phase separation into a number of small single-phase domains happens very quickly. The subsequent coarsening, by which like domains coalesce to form larger single-phase domains, then takes place over a much longer period. One such coarsening event can be seen in pane (a) around time $t \approx 2.5$ at $x \approx 15$. Note how the oil domains (red) are pushed along the direction of propagation for the wave until they coalesce into a single domain for all parameter values shown.

3.2 Results on a 2D spatial domain

We next present some 2D solutions to the problem for flow driven by acoustic forcing, from a SAW propagating along $z = 0$ in the positive x-direction. Similar to the 1D solutions, we start from a perturbed initial, constant concentration, on a square domain of size 20×20 in the (x, z)-plane (corresponding to a $2\,\text{cm} \times 2\,\text{cm}^2$), given by the initial condition

$$\phi(\vec{x}, 0) = \phi_0 + \sum_{j=1}^{N} \left(A_j \cos\left(\frac{2\pi j}{W} x\right) \cos\left(\frac{2\pi j}{W} z\right) + B_j \sin\left(\frac{2\pi j}{W} x\right) \sin\left(\frac{2\pi j}{W} z\right) \right),$$

$$p(\vec{x}, 0) = p_0 + \sum_{j=1}^{N} \left(A_j \cos\left(\frac{2\pi j}{W} x\right) \cos\left(\frac{2\pi j}{W} z\right) + B_j \sin\left(\frac{2\pi j}{W} x\right) \sin\left(\frac{2\pi j}{W} z\right) \right).$$

The parameters in the initial condition are as defined in the 1D case. Simulations were run for SAW amplitudes in the range $\mathcal{A} = 0.2{-}1.2$ nm. The results shared similar qualitative features, with the main differences being the time to reach a steady state and the shape of the interface between the two phases at the steady state. Figure 6 shows the steady state solutions for cases of small and large SAW amplitude. As we see in Fig. 6a, for the smallest SAW amplitude investigated, the water phase (blue) is strongly confined to the bottom-left corner of the computational domain, in contrast to the simulation for the largest SAW amplitude, where the water phase extends as a "tongue" toward the top right corner. Further, it takes the system twenty times as long to reach its steady state for the smaller amplitude SAW, $\mathcal{A} = 0.2$ nm, as compared with the larger amplitude, $\mathcal{A} = 1.2$ nm. Simulations for intermediate values of $\mathcal{A}$ confirm these trends, leading us to conclude that increasing SAW amplitude causes the system to reach equilibrium faster (quicker phase separation; see also Sect. 3.4) and the interface at equilibrium to be more distorted.

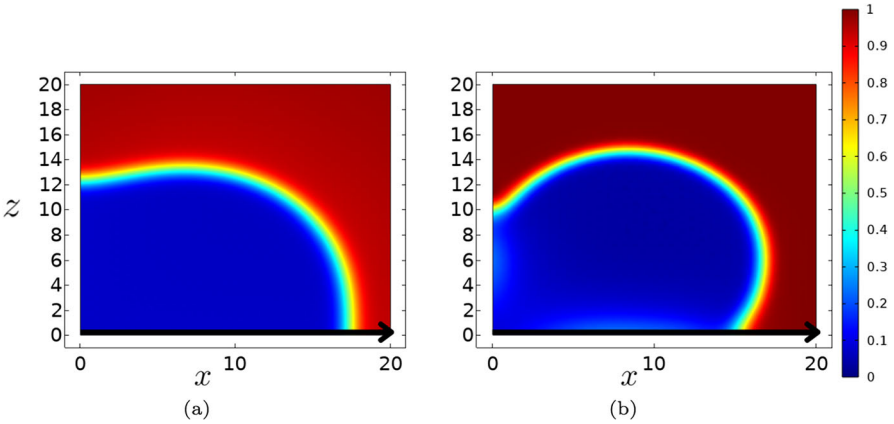

Fig. 6 The final concentration profiles, $\phi(x, z, t)$, at steady state, for the 2D problem driven by SAWs of amplitudes **a** $\mathcal{A} = 0.2$ nm and **b** $\mathcal{A} = 1.2$ nm, respectively, propagating along the positive x-axis. In **a**, equilibrium is reached at $t = 200$; in **b** at $t = 10$. Here, red indicates pure oil, while blue indicates pure water. The black arrow denotes the direction of propagation of the SAW along $z = 0$. (Color figure online)

Similar to the 1D results, we hypothesize that the resulting steady state solution is a result of the force being strongest in the bottom-left corner and directed at an angle to that corner, attenuating in both spatial directions from there. The water being the more mobile phase, it is pushed into this bottom-left corner, displacing the oil phase to other regions.

3.3 Results on a 3D spatial domain

We now discuss the most general case of simulations on a 3D dimensionless spatial domain occupying $(x, y, z) \in [0, 20]^3$ (corresponding to a cube of side length 2 cm), for either of the considered conservative volume forces acting on the mixture. In both simulations, the initial condition is a simple extension of our 1D and 2D cases:

$$\phi(\vec{x}, 0) = \phi_0 + \sum_{j=1}^{N} \left(A_j \cos\left(\frac{2\pi j}{W} x\right) \cos\left(\frac{2\pi j}{W} y\right) \cos\left(\frac{2\pi j}{W} z\right) + B_j \sin\left(\frac{2\pi j}{W} x\right) \sin\left(\frac{2\pi j}{W} y\right) \sin\left(\frac{2\pi j}{W} z\right) \right),$$

$$p(\vec{x}, 0) = p_0 + \sum_{j=1}^{N} \left(A_j \cos\left(\frac{2\pi j}{W} x\right) \cos\left(\frac{2\pi j}{W} y\right) \cos\left(\frac{2\pi j}{W} z\right) + B_j \sin\left(\frac{2\pi j}{W} x\right) \sin\left(\frac{2\pi j}{W} y\right) \sin\left(\frac{2\pi j}{W} z\right) \right).$$

We show just two representative simulations. Regarding the effects of gravity, Fig. 7 shows, as expected, that at short times the dynamics is dominated by the effects of

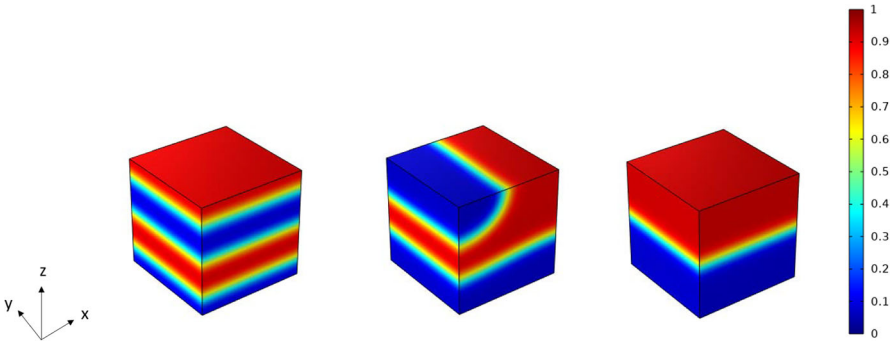

Fig. 7 Snapshots of the concentration profile, ϕ, with gravity acting on the system (represented by the potential $\psi_g = -\Lambda_g z$), shown at $t = 2, 90, 150$ (steady state). The computational domain is a cube of length 20. In the colorbar, red represents pure oil and blue pure water. (Color figure online)

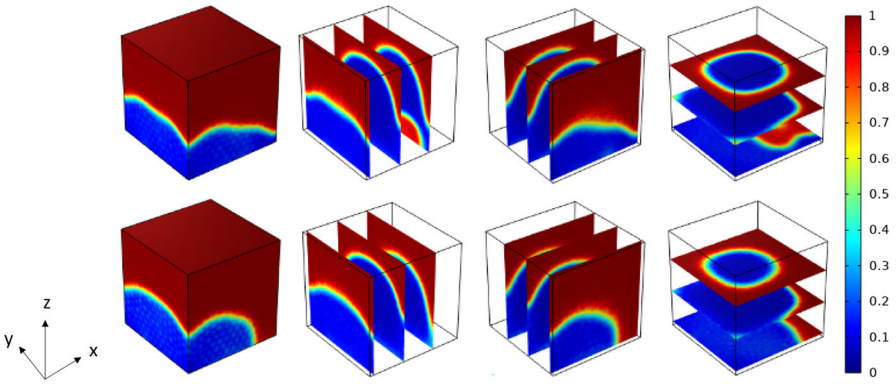

Fig. 8 Snapshots of the concentration profile, ϕ, with the potential from a SAW acting on the system, are shown at $t = 2$ in the first row and at $t = 12$ (steady state) in the second row. The first column shows the volume plots, while the subsequent columns show slices of this in the yz, xz, and xy planes, respectively. The computational domain is a cube of length 20

the Flory–Huggins logarithmic potential; this forces the initially well-mixed fluid to rapidly phase-separate into its constituent components. The small single-phase domains then coarsen until a single diffuse interface separates the two pure domains. Gravity (acting in the $(-z)$-direction) ensures that the less dense fluid (oil) rises atop the denser fluid (water) as was observed in the 1D simulation shown in Fig. 4.

Figure 8 shows the solution with the potential from a SAW acting on the system (same initial condition). The steady state solution is reached much more quickly for this case compared to the case of gravity. The dynamics still exhibit the same two qualitative regimes: initial rapid separation into small, pure component domains, which then coarsen over a longer time scale. In contrast to the gravity-driven case, we see here that the shape of the interface separating the two phases depends on all spatial coordinates and remains curved even at steady state, as was observed in our solutions to the 2D problem.

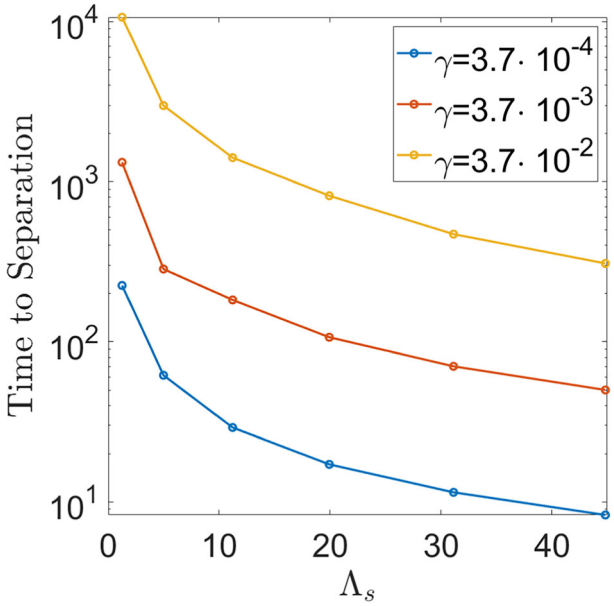

Fig. 9 The time to complete phase separation is plotted as a function of the nondimensional parameter Λ_s for three values of the dimensionless inverse attenuation length γ. The blue curve corresponds to the default value used in other simulations

In both cases, it was confirmed that we have a decreasing free energy functional and a conserved total fraction of oil in the mixture, in agreement with our analytic results.

3.4 Effect of SAW amplitude on time to phase separation

A possible application of SAW forcing on mixtures is to speed up phase separation of oil–water emulsions, thus it is important to quantify the extent to which this is possible. To attempt this, we carried out a number of 1D simulations at different SAW forcing strengths and measured the time to total phase separation (starting from the well-mixed initial state given by Eqs. (48), (49)). The results of this study are shown in Fig. 9, where we plot separation time versus the dimensionless parameter Λ_s that characterizes the strength of the SAW forcing (see Eqs. (20), (21) and Table 2).

Here, we calculate the total time to separation as the smallest time t such that the set $\mathcal{I} = \{x : \phi(x, t) = 0.5\}$ is a singleton, representing the time until only one interface exists. Experimental work done in our collaborator's lab utilizes systems where the maximum vertical displacements of the SAW, $\mathcal{A}$, are in the range [0.2, 1.2] nm, motivating the range of Λ_s values plotted in Fig. 9. We plot results for three values of the nondimensional parameter γ, which is the ratio between the attenuation length of the SAW in its direction of propagation (the x-direction) and the interfacial length scale. Assuming the interfacial length scale to be fixed, changes in γ then correspond to changes in the attenuation length (decreasing γ results in an increased attenuation

length; see Eq. (14)). Thus, as we would expect, decreasing γ results in less acoustic energy lost to the mixture, and thus a longer time to full phase separation, as Fig. 9 confirms. Further, as we have previously seen in Fig. 5, increasing the strength of the SAW, and hence increasing Λ_s, leads to a decrease in the time to phase separation. This is in qualitative agreement with the findings of Li et al. [16] that motivated our work; see their Fig. 5, which indicates an approximately exponential decay in the time to onset of phase separation with increasing SAW amplitude. However, such a comparison should be treated with caution; those authors study the more complicated problem of an emulsion drop on top of a substrate along which a SAW propagates. This setup is considerably more complicated than the one considered here, the presence of the free surface giving rise to additional effects such as surface tension, dynamic changes in the flow domain shape, and acoustic radiation pressure effects at the free surface, none of which are accounted for in our model.

On the other hand, our simulations can provide new insight into the relationship between attenuation length and time to phase separation, which is much more challenging to verify experimentally. We believe our findings are promising as, combined with the experimental evidence [16], they provide a sound theoretical proof-of-principle for using SAWs to enhance phase separation. We hope that our simplified modeling framework described by Eqs. (23)–(29) could provide a good starting-point for more detailed investigations to guide and optimize the experimental protocol.

4 Conclusions

In this work, we model and simulate the theoretical problem of a binary fluid mixture, trapped in a closed cell, excited by a conservative volume force. Our particular focus is on the application to a silicone oil–water mixture experiencing acoustic forcing from a SAW propagating through the underlying substrate. The mixture volume is assumed large enough that the main physical mechanism by which the SAW acts on the fluid is Eckart streaming [29–31].

The mathematical model is derived following an approach adapted from tumor modeling [4] using basic conservation and thermodynamic principles, leading ultimately to two coupled partial differential equations for the concentration of one phase (oil) and the fluid pressure, which we solve numerically. The free energy functional for the system is prescribed in accordance with the Cahn–Hilliard theory. This system, which utilizes a Darcy-type model for the velocities of each phase, offers a marked simplification over coupling the concentration equations for each phase to the full Navier-Stokes equations, yet, as our numerical results indicate, the model retains the necessary ingredients to model the desired physical effects, at least qualitatively.

While we consider that our model retains the most important physical effects, we note the following limitations: (i) all lengths are scaled with respect to the typical interfacial thickness, which is artificially increased so that simulations on the cm scale can be computed within a reasonable computing time; (ii) the model, as currently formulated, can only handle conservative external forces. With regard to modeling, the specific case of acoustic forcing considered here we also note that, due to the simplified geometry assumed, any effects associated with the presence of a free surface (such

as surface tension, dynamic shape change, acoustic radiation pressure) are neglected, limiting the applicability of our model.

We provide numerical solutions for the case of two different conservative volume forces acting on the mixture: gravity and acoustic forcing due to a SAW, each described by a potential function. The model predicts full phase separation in both cases, with the latter greatly decreasing the time necessary to achieve this in the experimentally relevant forcing regime. In all cases investigated, we can confirm that the total concentrations of both phases present are conserved, and that the underlying free energy of the system is nonincreasing, in agreement with analytical predictions. Although the acoustic forcing acts on both phases of the mixture, we speculate that the key to the enhanced phase separation lies in the very different mobilities of the two phases (the viscosity ratio of the considered fluids is 50:1), making the less viscous phase much easier to move. Unsurprisingly then, our model also predicts a decrease in time to phase separation as the SAW intensity (as characterized by the dimensionless parameter Λ_s) increases, and as the SAW attenuation length (characterized by γ^{-1}) decreases. Our future work, in collaboration with experimentalists, will be focused on improving the model to better represent the experimental setup, with a goal of making quantitative predictions.

Appendix A : Derivation of component velocity and flux equations

In this section, we propose equations for the fluxes $\vec{J}_i$ and the velocities $\vec{u}_i$ of each mixture component, following the approach adopted by Wise et al. [4], who develop a thermodynamically consistent diffuse-interface continuum model for a multiphase mixture representing a tumor growing in healthy tissue. To ensure consistency with the second law of thermodynamics, in the isothermal setting assumed here, it is necessary to obtain a nonincreasing free energy functional since this is equivalent to a nondecreasing entropy. For a binary mixture consisting of phases A, B at concentrations ϕ_A, ϕ_B, we assume a free energy $E = E[\phi_A, \phi_B]$. In the following, we assume the component densities ρ_A, ρ_B to be constant, allowing us to rewrite Eq. (6) as

$$\frac{\partial \phi_i}{\partial t} + \nabla \cdot (\phi_i \vec{u}_i) + \frac{1}{\rho_i} \nabla \cdot \vec{J}_i = 0, \qquad i = A, B. \tag{A.1}$$

Then, the rate of change of the free energy in time may be calculated as

$$\frac{\mathrm{d}E}{\mathrm{d}t} = \sum_{j=A}^{B} \int_\Omega \frac{\delta E}{\delta \phi_j} \frac{\partial \phi_j}{\partial t} \, \mathrm{d}\vec{x} \tag{A.2}$$

$$= \sum_{j=A}^{B} \int_\Omega \left(\phi_j \nabla \left(\frac{\delta E}{\delta \phi_j} + \tilde{p}_j \right) \cdot \vec{u}_j + \nabla \left(\frac{1}{\rho_j} \frac{\delta E}{\delta \phi_j} + \frac{1}{\rho_j} \tilde{p}_j \right) \cdot \vec{J}_j \right) \mathrm{d}\vec{x}$$

$$- \sum_{j=A}^{B} \int_{\partial\Omega} \frac{\delta E}{\delta \phi_j} \left[\frac{1}{\rho_j} \vec{J}_j + \vec{u}_j \phi_j \right] \cdot \hat{n} \, \mathrm{d}\vec{x}. \tag{A.3}$$

Here, Eq. (A.1) was used with $i = A,\ B$ to substitute for the time derivatives and then integration by parts was carried out, introducing the Lagrange multiplier $\tilde{p}_j$ to enforce the no-voids constraint of Eq. (7). The boundary terms arise from the integration by parts and are assumed to vanish; these serve as the boundary conditions for the numerical system solved in Sect. 3. From here, we choose to split the component velocities into two parts: a mass-averaged velocity, $\vec{u}$, and a diffusion velocity, $\vec{v}_j$, for $j = A, B$. We also introduce the pressure, p, and the potential (ψ) of a conservative volume force that is assumed to act, through the Lagrange multiplier as shown below,

$$p = \tilde{p}_j + \sum_{j=A}^{B} \phi_j \frac{\delta E}{\delta \phi_j} - \rho_j \psi \quad \text{and} \quad \vec{u}_j = \vec{u} + \vec{v}_j. \tag{A.4}$$

Making these substitutions and performing some algebraic manipulations then yields

$$\begin{aligned}
\frac{\mathrm{d}E}{\mathrm{d}t} = \sum_{j=A}^{B} \Bigg\{ & \int \phi_j \nabla \left(\frac{\delta E}{\delta \phi_j} + p - \sum_{i=1}^{2} \phi_i \frac{\delta E}{\delta \phi_i} + \rho_j \psi \right) \cdot \vec{u} \, \mathrm{d}\vec{x} \\
& + \int \phi_j \nabla \left(\frac{\delta E}{\delta \phi_j} + p - \sum_{i=A}^{B} \phi_i \frac{\delta E}{\delta \phi_i} + \rho_j \psi \right) \cdot \vec{v}_j \, \mathrm{d}\vec{x} \\
& + \int \nabla \left(\frac{1}{\rho_j} \frac{\delta E}{\delta \phi_j} + \frac{1}{\rho_j} \left(p - \sum_{i=A}^{B} \phi_i \frac{\delta E}{\delta \phi_i} + \rho_j \psi \right) \right) \cdot \vec{J}_j \, \mathrm{d}\vec{x} \Bigg\}
\end{aligned} \tag{A.5}$$

$$\begin{aligned}
= & \int \sum_{j=A}^{B} \left\{ \phi_j \left(\nabla \frac{\delta E}{\delta \phi_j} + \nabla p - \sum_{i=A}^{B} \phi_i \nabla \frac{\delta E}{\delta \phi_i} - \sum_{i=A}^{B} \frac{\delta E}{\delta \phi_i} \nabla \phi_i + \rho_j \nabla \psi \right) \cdot \vec{u} \, \mathrm{d}\vec{x} \right\} \\
& + \sum_{j=A}^{B} \Bigg\{ \int \phi_j \nabla \left(\frac{\delta E}{\delta \phi_j} + p - \sum_{i=A}^{B} \phi_i \frac{\delta E}{\delta \phi_i} + \rho_j \psi \right) \cdot \vec{v}_j \, \mathrm{d}\vec{x} \\
& + \int \nabla \left(\frac{1}{\rho_j} \frac{\delta E}{\delta \phi_j} + \frac{1}{\rho_j} \left(p - \sum_{i=A}^{B} \phi_i \frac{\delta E}{\delta \phi_i} + \rho_j \psi \right) \right) \cdot \vec{J}_j \, \mathrm{d}\vec{x} \Bigg\}.
\end{aligned} \tag{A.6}$$

Next, the no-voids constraint allows us to recast the system in terms of a single concentration variable $\phi = \phi_A$, $1 - \phi = \phi_B$; in addition, it must be true that the component fluxes are equal and opposite, $-\vec{J}_A = \vec{J}_B$, in order to satisfy mass conservation of the mixture. Utilizing these facts, Eq. (A.6) is simplified to

$$\begin{aligned}
\frac{\mathrm{d}E}{\mathrm{d}t} = & \int \left(\nabla p - 2 \frac{\delta E}{\delta \phi} \nabla \phi + \rho_{\mathrm{m}} \nabla \psi \right) \cdot \vec{u} \, \mathrm{d}\vec{x} \\
& + \sum_{j=A}^{B} \left\{ \int \phi_j \left(\nabla \frac{\delta E}{\delta \phi_j} + \nabla p + (1 - 2\phi) \nabla \frac{\delta E}{\delta \phi} - 2 \frac{\delta E}{\delta \phi} \nabla \phi + \rho_j \nabla \psi \right) \cdot \vec{v}_j \, \mathrm{d}\vec{x} \right\} \\
& + \int \left(\left(\frac{1}{\rho_A} + \frac{1}{\rho_B} \right) \nabla \frac{\delta E}{\delta \phi} + \left(\frac{1}{\rho_A} - \frac{1}{\rho_B} \right) \left(\nabla p + (1 - 2\phi) \nabla \frac{\delta E}{\delta \phi} - 2 \frac{\delta E}{\delta \phi} \nabla \phi \right) \right)
\end{aligned}$$

$$\cdot \vec{J}_A \, \mathrm{d}\vec{x}. \tag{A.7}$$

Thus, if we let

$$\vec{u} = -q \left(\nabla p - 2\frac{\delta E}{\delta \phi} \nabla \phi + \rho_{\mathrm{m}} \nabla \psi \right), \tag{A.8}$$

$$\vec{v}_j = -q_j \left(\nabla \frac{\delta E}{\delta \phi_j} + \nabla p + (1-2\phi) \nabla \frac{\delta E}{\delta \phi} - 2\frac{\delta E}{\delta \phi} \nabla \phi + \rho_j \nabla \psi \right), \tag{A.9}$$

$$\vec{J}_A = -M_B \left(\left(\frac{1}{\rho_A} + \frac{1}{\rho_B} \right) \nabla \frac{\delta E}{\delta \phi} + \left(\frac{1}{\rho_A} - \frac{1}{\rho_B} \right) \left(\nabla p + (1-2\phi) \nabla \frac{\delta E}{\delta \phi} - 2\frac{\delta E}{\delta \phi} \nabla \phi \right) \right), \tag{A.10}$$

where $q, q_j, M_B \geq 0$ are positive mobility coefficients, then we obtain

$$\frac{\mathrm{d}E}{\mathrm{d}t} = -\int \frac{1}{q} |\vec{u}|^2 + \sum_{j=A}^{B} \frac{\phi_j}{q_j} |\vec{v}_j|^2 + \frac{1}{M_B} |\vec{J}_A|^2 \, \mathrm{d}\vec{x} < 0. \tag{A.11}$$

Hence, with these assumptions, the component velocities are given by

$$\vec{u}_A = -(q + q_A) \left[\nabla p - 2\frac{\delta E}{\delta \phi} \nabla \phi \right] - q \rho_{\mathrm{m}} \nabla \psi - q_A \left[2(1-\phi) \nabla \frac{\delta E}{\delta \phi} + \rho_1 \nabla \psi \right], \tag{A.12}$$

$$\vec{u}_B = -(q + q_B) \left[\nabla p - 2\frac{\delta E}{\delta \phi} \nabla \phi \right] - q \rho_{\mathrm{m}} \nabla \psi - q_B \left[\rho_2 \nabla \psi - 2\phi \nabla \frac{\delta E}{\delta \phi} \right]. \tag{A.13}$$

Appendix B : Computational implementation

Equations (23)–(29) are written in a form convenient for the use of COMSOL™Multiphysics PDE Coefficients Form. This package solves, by finite elements, a vectorial equation for the unknown vector $\vec{v} = (v_1, v_2, \ldots, v_N)^\top$. The equation is of the form

$$\mathbf{e} \frac{\partial^2 \vec{v}}{\partial t^2} + \mathbf{d} \frac{\partial \vec{v}}{\partial t} + \nabla \cdot (-\mathbf{c} \nabla \vec{v} - \alpha \, \vec{v} + \gamma) + \beta \, \nabla \vec{v} + \mathbf{a} \, \vec{v} = \vec{f}, \tag{B.1}$$

where the coefficients of the N scalar equations are in the matrices $\mathbf{e}$, $\mathbf{d}$, γ, $\mathbf{a}$ (of dimensions $N \times N$), α, β (of dimensions $N \times N \times n$), $\mathbf{c}$ (of dimensions $N \times N \times n \times n$) and the vector $\vec{f}$ (of dimension N), where n is the spatial dimension of the problem ($n = 1, 2, 3$). In index notation, this equation reads as

$$e_{ij} \frac{\partial^2 v_j}{\partial \tilde{t}^2} + d_{ij} \frac{\partial v_j}{\partial \tilde{t}} + \frac{\partial}{\partial \tilde{x}_l} \left(-c_{ijkl} \frac{\partial v_j}{\partial \tilde{x}_k} - \alpha_{ijl} v_j + \gamma_{il} \right) + \beta_{ijl} \frac{\partial v_j}{\partial \tilde{x}_l} + a_{ij} v_j = f_i, \tag{B.2}$$

where $i, j = 1\ldots., N$ and $k, l = 1, \ldots, n$.

Here, we briefly describe the scheme to solve the 1D problem. The considered system given by Eqs. (23)–(29) is rewritten in terms of the quantities $\vec{v} = (\phi, p, \mu, u_A, u_B, J_A, P)^T$. Thus, we use seven equations (for $n = 1$), corresponding to the solution depending on a single spatial variable x. In the following, we list the non-vanishing coefficients (we omit the indexes k and l for brevity and consider $x_1 = x$ since $k = l = 1$):

- Row 1 ($i = 1$) for Eq. (23)

$$d_{11} = 1, \quad \alpha_{14} = -\phi, \quad \alpha_{16} = -\frac{1}{R_\rho}. \tag{B.3}$$

- Row 2 ($i = 2$) for Eq. (24)

$$\alpha_{24} = -\phi, \quad \alpha_{25} = \phi - 1, \quad \alpha_{26} = \frac{R_\rho - 1}{R_\rho}. \tag{B.4}$$

- Row 3 ($i = 3$) for Eq. (25)

$$c_{31} = -1, \quad a_{33} = 1, \quad f_3 = f'(\phi) + (R_\rho - 1)\Lambda\psi. \tag{B.5}$$

- Row 4 ($i = 4$) for Eq. (26)

$$\begin{aligned} a_{41} = \kappa\Lambda(R_\rho - 1)\frac{\partial\psi}{\partial x}, \quad a_{44} = 1, \quad a_{47} = (\kappa_1 + \kappa), \\ \beta_{43} = 2\kappa_1(1 - \phi), \quad f_4 = -\Lambda(\kappa + \kappa_1 R_\rho)\frac{\partial\psi}{\partial x}. \end{aligned} \tag{B.6}$$

- Row 5 ($i = 5$) for Eq. (27)

$$\begin{aligned} a_{51} = \kappa\Lambda(R_\rho - 1)\frac{\partial\psi}{\partial x}, \quad a_{55} = 1, \quad a_{57} = (1 + \kappa_1), \\ \beta_{53} = -2\phi, \quad f_5 = -\Lambda(\kappa + 1)\frac{\partial\psi}{\partial x}. \end{aligned} \tag{B.7}$$

- Row 6 ($i = 6$) for Eq. (28)

$$a_{66} = 1, \quad a_{67} = \mathcal{M}\left(\frac{1 - R_\rho}{R_\rho}\right), \quad \beta_{63} = \frac{2\mathcal{M}}{R_\rho}(1 - \phi + R_\rho\phi). \tag{B.8}$$

- Row 7 ($i = 7$) for Eq. (29)

$$a_{71} = 1, \quad \beta_{71} = 2\mu, \quad \beta_{72} = -1. \tag{B.9}$$

At the domain ends, we apply Dirichlet boundary conditions $p = 0$ in conjunction with the Flux/Source boundary condition that exactly matches Eqs. (31)–(32) with this definition of $\vec{v}$.

Acknowledgements This work was supported by the donors of ACS Petroleum Research Fund under PRF# 62062-ND9 and by BSF grant No. 2020174. J.A.D. acknowledges support from Consejo Nacional de Investigaciones Científicas y Técnicas (CONICET, Argentina) with Grant PIP 02114-CO/2021 and Agencia Nacional de Promoción Científica y Tecnológica (ANPCyT, Argentina) with Grant PICT 02119/2020.

Author contributions M.F., L.C., and L.K. wrote the manuscript text and M.F. prepared the figures. J.D. was instrumental in helping to design the numerical model. O.M. provided significant insights into modeling SAW effects and interpreting results. All authors reviewed the manuscript.

Data availability No datasets were generated or analyzed during the current study.

Declarations

Conflict of interest The authors declare no competing interests.

References

1. Favazza C, Kalyanaraman R, Sureshkumar R (2006) Robust nanopatterning by laser-induced dewetting of metal nanofilms. Nanotechnology. https://doi.org/10.1088/0957-4484/17/16/038
2. Khor CS, Akinbola G, Shah N (2020) A model-based optimization study on greywater reuse as an alternative urban water resource. Sustain Prod Consum 22:186–194
3. Kuang X, Guan G, Wong MK, Chan LY, Zhao Z, Tang C, Zhang L (2022) Computable early *Caenorhabditis elegans* embryo with a phase field model. PLoS Comput Biol. https://doi.org/10.1371/journal.pcbi.1009755
4. Wise SM, Lowengrub JS, Frieboes HB, Cristini V (2008) Three-dimensional multispecies nonlinear tumor growth-I: model and numerical method. J Theor Biol 253:524–543
5. Anderson DM, McFadden GB, Wheeler AA (1998) Diffuse-interface methods in fluid mechanics. Annu Rev Fluid Mech 30:139–165
6. Cahn JW, Hilliard JE (1958) Free energy of a nonuniform system. 1. Interfacial free energy. J Chem Phys 28:258
7. Cahn JW, Hilliard JE (1959) Free energy of a nonuniform system. III. Nucleation in a two-component incompressible fluid. J Chem Phys 31:688–699
8. Dedè L, Quarteroni A (2018) Isogeometric analysis of a phase field model for Darcy flows with discontinuous data. Chin Ann Math Ser B 39:487–512
9. Cavaterra C, Frigeri S, Grasselli M (2021) Nonlocal Cahn–Hilliard–Hele–Shaw systems with singular potential and degenerate mobility. J Math Fluid Mech. https://doi.org/10.1007/s00021-021-00648-1
10. Giorgini A, Lam K, Rocca E, Schimperna G (2022) On the existence of strong solutions to the Cahn–Hilliard–Darcy system with mass source. SIMA 54:737–767
11. Khatavkar VV, Anderson PD, Meijer HEH (2006) On scaling of diffuse-interface models. Chem Eng Sci 61:2364–2378
12. Náraigh LO, Thiffeault J-L (2010) Nonlinear dynamics of phase separation in thin films. Nonlinearity 23:1559–1583
13. Ding H, Spelt P, Shu C (2007) Diffuse interface model for incompressible two-phase flows with large density ratios. J Comput Phys 226:2078–2095
14. Thiele U (2018) Recent advances in and future challenges for mesoscopic hydrodynamic modelling of complex wetting. Colloids Surf A Physiochem Eng Asp 553:487–495

15. Thiele U, Archer AJ, Pismen LM (2016) Gradient dynamics models for liquid films with soluble surfactant. Phys Rev Fluids 1:083903
16. Li Y, Marcos JM, Fasano M, Diez JA, Cummings L, Kondic L, Manor O (2025) Using wetting and ultrasonic waves to extract oil from oil/water mixtures. Preprint at arXiv:2502.08800
17. Rezk AR, Manor O, Friend JR, Yeo LY (2012) Unique fingering instabilities and soliton-like wave propagation in thin acoustowetting films. Nat Commun 3:1167–1173
18. Altshuler G, Manor O (2015) Spreading dynamics of a partially wetting water film atop a MHz substrate vibration. Phys Fluids 27:102103
19. Horesh A, Khaikin D, Karnilaw M, Zigelman A, Manor O (2019) Acoustogravitational balance in climbing films. Phys Rev Fluids 4:022001
20. Rezk AR, Manor O, Yeo LY, Friend JR (2014) Double flow reversal in thin liquid films driven by megahertz-order surface vibration. Proc R Soc A. https://doi.org/10.1098/rspa.2013.0765
21. Mogilner A, Manhart A (2018) Intracellular fluid mechanics: coupling cytoplasmic flow with active cytoskeletal gel. Annu Rev Fluid Mech 50:347–370
22. Shiokawa S, Matsui Y, Ueda T (1989) Liquid streaming and droplet formation caused by leaky Rayleigh waves. In: Proceedings of IEEE ultrasonics symposium, vol 1, pp 643–646. https://doi.org/10.1109/ULTSYM.1989.67063
23. Li Y, Diez JA, D'Addesa J, Manor O, Cummings LJ, Kondic L (2023) Thin films spreading under the action of surface acoustic waves. arXiv Preprint. arXiv:2312.12367
24. Arzt R, Salzmann E (1967) Elastic surface waves in quartz at 316 MHz. Appl Phys Lett 10:165–167
25. Badalassi VE, Ceniceros HD, Banerjee S (2003) Computation of multiphase systems with phase field models. J Comput Phys 190:371–397
26. Flory PJ (1944) Thermodynamics of heterogeneous polymers and their solutions. J Chem Phys 12:425–438
27. Lee D, Huh J-Y, Jeong D, Shin J, Yun A, Kim J (2014) Physical, mathematical, and numerical derivations of the Cahn–Hilliard equation. Comput Mater Sci 81:216–225
28. Diez JA, Gonzalez AG, Garfinkel DA, Rack PP, Mckeown JT, Kondic L (2021) Simultaneous decomposition and dewetting of nanoscale alloys: a comparison of experiment and theory. Langmuir 37:2575
29. Eckart C (1948) Vortices and streams caused by sound waves. Phys Rev 73:68–76
30. Lighthill J (1978) Acoustic streaming. J Sound Vib. 61:391–418
31. Friend J, Yeo LY (2011) Microscale acoustofluidics: microfluidics driven via acoustics and ultrasonics. Rev Mod Phys 83:647–704